Available online at www.sciencedirect.com
ScienceDirect
Journal of Computational Physics 217 (2006) 295–311
JOURNAL OF COMPUTATIONAL PHYSICS
www.elsevier.com/locate/jcp

# A level set approach to simulate magnetohydrodynamic-instabilities in aluminum reduction cells

David Munger *, Alain Vincent

*Département de physique, Université de Montréal, C.P. 6128, succ. centre-ville, Montréal, Que., Canada H3C 3J7*

Received 7 September 2005; received in revised form 29 December 2005; accepted 3 January 2006
Available online 8 February 2006

**Abstract**

Magnetohydrodynamic instabilities at the metal-bath interface in aluminum reduction cells is an important and not fully understood topic. To simulate the two-fluid three-dimensional unstationary flow subject to a background magnetic field, a level set approach is proposed. It features a formulation in terms of the magnetic vector potential to avoid a numerical growth of the divergence of the magnetic field. The same exact projection scheme (with staggered grids) is used for both the velocity field and the magnetic vector potential. Test simulations show that the overall method behaves well in purely hydrodynamic as well as in fully magnetohydrodynamic regimes, in both cases with a single fluid and with two fluids. We also simulate with our technique the metal pad roll instability and trace the behavior of coupled interfacial modes.


*Keywords:* Magnetohydrodynamics; Instability; Aluminum reduction cell; Metal pad roll; Magnetic vector potential; Numerical simulation; Level set method; Finite volumes

## 1. Introduction

Industrial production of aluminum is achieved by means of electrolysis of alumina, an aluminum oxide [1]. The latter is dissolved into a thin layer of electrolytic bath, lying on top of a liquid aluminum layer of 8.6% higher density inside a rectangular cell (see Fig. 1). The horizontal dimensions of the cell are around 10 m × 4 m, while each liquid layer is only about 20 cm thick. Since the electrolysis current, of 400 kA in modern cells, is carried out downward through the bath, strong Joule heating occurs, maintaining the temperature of the system around 960 °C, that is, well over the fusion point of aluminum. Such aluminum reduction cells are lined up into a smelter and connected together in series by bus bars. A background magnetic field is therefore induced over the cells; its intensity and orientation depend on the placement of the bus bars.

This two-liquid layer system has been observed to be subject to interfacial instabilities driven by magnetic forces [2–5]. Since the bath is $10^4$ times more resistive than liquid aluminum, the electric current, which tends to flow through the least resistive paths, is very sensitive to the motion of the aluminum–bath interface. Thus,

* Corresponding author. Tel.: +1 514 343 3219; fax: +1 514 343 2071.
*E-mail addresses:* david.munger@umontreal.ca (D. Munger), vincent@astro.umontreal.ca (A. Vincent).

0021-9991/$ - see front matter 
doi:10.1016/j.jcp.2006.01.002

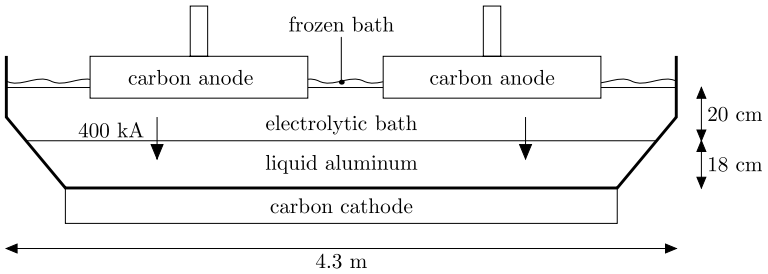


Fig. 1. Vertical cut of a Hall–Héroult cell.

the vertical electrolysis current is diverted horizontally upon a displacement of the interface, and a magnetic force arises from the interaction between these new current components and the vertical component of the background magnetic field. This is the basis of the instability mechanism of a rotating wave known as the metal pad roll, that has been extensively studied theoretically [6–9] and proven to follow from the coupling between different oscillation modes by the magnetic force.

Owing to the high temperature inside the cell, experimental data are hardly obtained and are limited, to our knowledge, to the measurement of the erosion of iron rods by the flow [1], of radioactive tracers and of anodic currents intensity [10]. So far, a direct observation of the interface motion is impossible. Thus, numerical simulation turns out to be a useful tool to investigate magnetohydrodynamic (MHD) instabilities in aluminum reduction cells.

Various two-dimensional models resulting from more or less strong approximations have been used for numerical computations [11]. However, only a few direct three-dimensional simulations have been carried out in the past, by Potočnik [12] using the finite elements industrial code ESTER/PHOENICS, and by Gerbeau and coworkers [13], who developed their own, mathematically rigorous, arbitrary Lagrangian–Eulerian (ALE) numerical method. This consists in a finite elements-like grid discretization. It requires the interface not to be altered by strong topological changes, but has the advantage of being able to handle strong discontinuities at the interface.

Like the ALE approach, the model we propose in this study relies on as little simplifying assumptions as possible. We first discuss the equations that model the physics in a Hall–Héroult cell. Next, we explain the way the interface is treated using a level set method. Then we give the details of the space–time discretization of our model. At last, a few numerical tests with our code are reported, as well as a simulation of the metal pad roll.

## 2. Physical model

We focus on the physical mechanisms that are independent of the geometrical peculiarities of the cell, such as the inclined ledges near the bottom of the cell and the open channels between the anodes [3,14]. Thus, we consider the simplified geometry depicted in Fig. 2: a single anode spanning over all the top of the cell, with purely vertical walls. During the reduction reaction, the oxygen from the alumina combines to the carbon

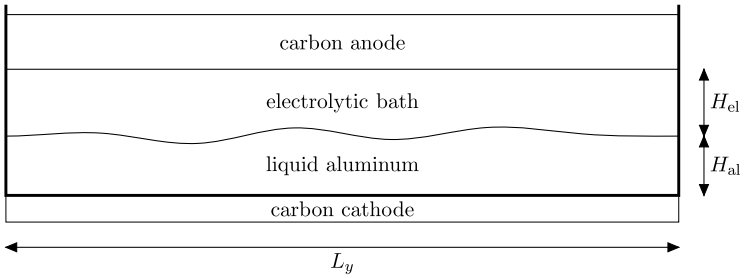


Fig. 2. Simplified geometry.

from the anodes to form carbon oxides. Our model does not account for those, unlike in the model of Potočnik [12], nor for the frozen bath that gathers on the ledges. We rather consider insulating vertical walls.

We solve the three-dimensional unsteady incompressible MHD equations of transport, using a formulation in terms of the magnetic vector potential.

### 2.1. Mass and momentum transport

Momentum transport is modeled by the Navier–Stokes equation [15], comprising buoyancy and magnetic effects in the last two terms:

$$\frac{\partial \rho \vec{v}}{\partial t} = -\vec{\nabla} p - \vec{\nabla} \cdot (\rho \vec{v}\,\vec{v} - 2\rho \nu D) + \vec{F}_{\mathrm{g}} + \vec{F}_{\mathrm{m}}, \tag{1}$$

where $\vec{v}$ is the flow velocity and $\rho$ is the mass density. The first term on the right-hand side is the gradient of total pressure, including thermodynamic, hydrostatic and magnetostatic pressures, and is determined by the incompressibility condition

$$\vec{\nabla} \cdot \vec{v} = 0$$

on mass conservation. Within the parentheses of Eq. (1) are the inertia and viscous terms respectively, where $D = \frac{1}{2}[\vec{\nabla}\vec{v} + (\vec{\nabla}\vec{v})^{\mathrm{T}}]$ is the strain rate tensor and $\nu$ is the kinematic viscosity.

The total gravitational force density is $-\rho g \vec{e}_z$, where $g$ is the gravitational acceleration. But, defining $\rho_0(z)$ as the equilibrium density profile, the total force is split into an hydrostatic pressure gradient $\vec{\nabla}(-\int \rho_0 g \,\mathrm{d}z)$ and the buoyancy force density

$$\vec{F}_{\mathrm{g}} = -(\rho - \rho_0) g \vec{e}_z, \tag{2}$$

which is null at equilibrium. When the system is static, the interface is flat and stands at, say, $z = H_{\mathrm{al}}$; then $\rho_0$ is set to the liquid metal density for $z < H_{\mathrm{al}}$ and to the bath density otherwise.

We apply a similar treatment to the total magnetic force density $\vec{J} \times \vec{B}$, where $\vec{J}$ and $\vec{B}$ denote the electric current and magnetic flux densities, respectively. Due to its complexity, this task deserves its own section.

### 2.2. Magnetic force

Our aim here is to decompose the magnetic force into components with different physical meanings, in order to make some simplification, but also to allow a better investigation of the physical processes.

We first begin with splitting the electric current density into the imposed vertical current $\vec{J}_0 = -J_0 \vec{e}_z$ and a disturbance $\vec{j}$ from equilibrium, each of them inducing some magnetic flux, with corresponding densities $\vec{B}_0$ and $\vec{b}$. Then we add the background magnetic induction due to remote currents $\vec{B}_{\mathrm{bg}}$, yet unspecified, so that

$$\vec{B} = \vec{B}_{\mathrm{bg}} + \vec{B}_0 + \vec{b}. \tag{3}$$

Next, we have to guess the form of $\vec{B}_0$. Though a rigorous analysis would require computing it from Biot–Savart's law, this would lead to a needlessly complex solution. So, following [4,5], we set $\vec{B}_0$ to a simpler linear expression such that $\vec{\nabla} \times \vec{B}_0 = \mu_0 \vec{J}_0$ according to Ampère's law:

$$\vec{B}_0 = \frac{\mu_0 J_0}{2}\left[\left(y - \frac{L_y}{2}\right)\vec{e}_x - \left(x - \frac{L_x}{2}\right)\vec{e}_y\right].$$

This field, nevertheless, may not be induced solely by the current density $\vec{J}_0$. Indeed, the difference between this expression and the exact solution to Biot–Savart's law can be regarded as a residual part of the background field, which does not appear in the original definition of $\vec{B}_{\mathrm{bg}}$. Next, we require that $\vec{B}_0$ induce no motion at equilibrium [4], but it is readily verified that $\vec{J}_0 \times \vec{B}_0$ can be written as the gradient of a quantity that we shall call the magnetostatic pressure. The latter can be obtained from direct calculations, but needs not be detailed here. It should be noted that the vertical component of the background field cannot generate motion at equilibrium. Nevertheless, it has to be irrotational so that it is not associated with local currents.

On account of the previous discussion, we consider the following expression for the effective magnetic force:

$$\vec{F}_{\mathrm{m}} = \vec{J}_0 \times (\vec{B}_{\mathrm{bg}} + \vec{b}) + \vec{j} \times \vec{B} \tag{4}$$

with $\vec{B}$ given by Eq. (3), and under the constraint $\vec{\nabla} \times \vec{B}_{\mathrm{bg}} = 0$.

### 2.3. Magnetic field evolution

Under the assumption that no high-frequency electromagnetic waves would stand in a sufficiently conducting medium, the displacement currents can be neglected in Ampère's law [16] and this leads to the magnetohydrodynamic approximation:

$$\vec{\nabla} \times \vec{B} \cong \mu_0 \vec{J}, \tag{5}$$

where $\mu_0$ is the magnetic permeability of void (nearly that of liquid aluminum). It can be further shown that, under the same assumptions, the electric force can also be neglected [16] in the Navier–Stokes equation, which results in Eq. (1). The current disturbance in Eq. (4) is computed, according to Eq. (5), as $\vec{j} = \vec{\nabla} \times \vec{b}/\mu_0$.

Combining Eq. (5) with Faraday's and Ohm's laws to eliminate the electric field yields the following evolution equation for the magnetic induction field:

$$\frac{\partial \vec{B}}{\partial t} = \vec{\nabla} \times (\vec{v} \times \vec{B} - \eta \vec{\nabla} \times \vec{B}). \tag{6}$$

The first term on the right-hand side stands for transport and stretching by the flow, while the second one basically corresponds to magnetic diffusion by Joule heating, with its coefficient defined as the magnetic diffusivity $\eta = 1/\mu_0\sigma$. Some additional meaning hidden into this term will be revealed in the following section.

Besides, the magnetic field must remain (from Maxwell's equations) solenoidal:

$$\vec{\nabla} \cdot \vec{B} = 0, \tag{7}$$

which of course excludes magnetic monopoles. It is straightforward to show, by taking the divergence of Eq. (6), that $\vec{B}$ remains divergence-free if $\vec{B}(t = 0)$ satisfies Eq. (7). However, the numerical resolution of Eq. (6) does not preserve this property in general. This is indeed a well-known problem commonly dealt with by using a projection step [17], which turned out to be inefficient in our case [18], rather leading the flow to an obviously non-physical regime. To overcome this difficulty, divergence cleaning algorithms [19,20] have been proposed. Here, we chose instead to replace the magnetic field with its vector potential $\vec{A}$, thus ensuring $\vec{\nabla} \cdot \vec{B} = 0$ implicitly [21].

### 2.4. Magnetic vector potential formulation

In virtue of Helmholtz's theorem, the magnetic vector potential $\vec{a}$ is uniquely defined by

$$\vec{\nabla} \times \vec{a} = \vec{b}$$

together with a gauge condition, i.e. a constraint on $\vec{\nabla} \cdot \vec{a}$, and suitable boundary conditions. Setting $\vec{\nabla} \cdot \vec{a} = 0$, an evolution equation for the potential $\vec{a}$ is obtained:

$$\frac{\partial \vec{a}}{\partial t} = -\vec{\nabla}\varphi + \vec{v} \times (\vec{B}_{\mathrm{bg}} + \vec{B}_0 + \vec{\nabla} \times \vec{a}) + \eta \nabla^2 \vec{a} - (\eta - \eta_0)\mu_0 \vec{J}_0, \tag{8}$$

where $\varphi$, the time-dependent part of the electric potential that adjusts to make the current disturbance form closed loops, is determined by the gauge condition. The magnetic diffusivity profile at equilibrium $\eta_0(z)$, constructed in the same manner as $\rho_0(z)$ in Section 2.1, is included so that $\partial \vec{a}/\partial t = 0$ at equilibrium when $\vec{v} = 0$ and $\vec{a} = 0$. It is readily verified that taking the curl of this equation leads back to Eq. (6).

Observing that

$$\nabla^2 \vec{a} = -\mu_0 \vec{j}, \tag{9}$$

it is easily understood that the third term in Eq. (8) corresponds to the diffusion of the field induced by local current disturbances. The last term in Eq. (8) deserves some explanation. As opposed to the third one, it is associated to the undisturbed electrolysis current $\vec{J}_0$, and furthermore it is null at equilibrium. Thus, it can

only act through changes of the gradient of electrical conductivity that appear upon a displacement of the aluminum–bath interface. Only the rotational part of this term is physically meaningful; it symbolically writes down as:

$$\mu_0 J_0 \left[ (\eta - \eta_0)\vec{e}_z - \nabla^{-2} \frac{\partial}{\partial z} \vec{\nabla}(\eta - \eta_0) \right].$$

Its contribution to the current can be obtained using Eq. (9):

$$\frac{\partial \vec{j}}{\partial t} = \cdots - J_0 \nabla_{\mathrm{h}}^2 (\eta - \eta_0)\vec{e}_z + J_0 \frac{\partial}{\partial z} \vec{\nabla}_{\mathrm{h}} (\eta - \eta_0), \tag{10}$$

where $\vec{\nabla}_{\mathrm{h}}$ is the horizontal projection of the gradient operator, and $\nabla_{\mathrm{h}}^2 = \vec{\nabla}_{\mathrm{h}} \cdot \vec{\nabla}_{\mathrm{h}}$. This expression is divergence-free, so the diverted currents form closed loops.

Before pushing this analysis any further, we emphasize that even if, at first sight, it does not make sense to take derivatives across the discontinuity at the interface, we are using, as described in Section 3, a level set method in which the jump in conductivity is made smooth. From now on, all discontinuities shall be assumed to be smooth. To illustrate the behavior of the right-hand side of Eq. (10), we consider a bump into the interface, i.e. a zone where the bath is replaced with aluminum, which appears as a hole in the (smooth) function $\eta - \eta_0$. This means that $\nabla_{\mathrm{h}}^2(\eta - \eta_0) > 0$, and from the $z$-component of Eq. (10), we see that the diverted currents flow down through the bump, which is in agreement with the fact that the current prefers the least resistive paths.

To summarize, the last term of Eq. (8) is at the origin of the current diversion by displacements of the aluminum–bath interface. Second-order effects are relayed to the $\eta \nabla^2 \vec{a}$ term. A last remark should be made about the fact that this vector potential formulation has the drawback of involving higher-order derivatives in the equations. But this is not a problem here, since $\vec{a}$ remains pretty smooth because of the strong magnetic diffusion.

### 2.5. Scaling

The physical variables are made non-dimensional using the following units:

- the magnetic force characteristic propagation time $T_0 \equiv \tau_{\mathrm{m}} = 5.96$ s as the unit time, defined in Table 1;
- the vertical anode–cathode distance $L_0 \equiv L_z = 38.0$ cm as the unit length;
- the corresponding speed $U_0 \equiv L_0/T_0 = 6.37$ cm/s at the unit velocity;
- the density $\rho_{\mathrm{el}} = 2090$ kg/m$^3$ of the electrolytic bath as the unit density;
- the intensity $J_0 = 400$ kA of the imposed current as the unit electric current;
- the corresponding magnitude $\mu_0 J_0 L_0 = 3.27$ mT of the induced field as the unit magnetic induction, implying $(\mu_0 J_0 L_0) \times L_0 U_0 = 7.92$ mV for the electric potential.

This choice results in the following non-dimensional forms of Eqs. (1) and (8):

$$\frac{\partial \rho \vec{v}}{\partial t} = -\vec{\nabla} p - \vec{\nabla} \cdot \left( \rho \vec{v}\,\vec{v} - \frac{2\rho D}{Re} \right) - \frac{\vec{F}_{\mathrm{g}}}{Fr^2} + \vec{F}_{\mathrm{m}}, \tag{11}$$

$$\frac{\partial \vec{a}}{\partial t} = -\vec{\nabla}\varphi + \vec{v} \times (\vec{B}_{\mathrm{bg}} + \vec{B}_0 + \vec{\nabla} \times \vec{a}) + \frac{1}{\mathrm{Rm}} \nabla^2 \vec{a} + \left( \frac{1}{\mathrm{Rm}} - \frac{1}{\mathrm{Rm}_0} \right) \vec{e}_z, \tag{12}$$

Table 1
Characteristic times

| Time | Symbol | Definition |
|---|---|---|
| Magnetic diffusion | $\tau_\eta$ | $L_0^2/\eta$ |
| Buoyancy | $\tau_{\mathrm{g}}$ | $\sqrt{\rho_{\mathrm{el}} L_0 / \Delta\rho g}$ |
| Magnetic force | $\tau_{\mathrm{m}}$ | $\sqrt{\rho_{\mathrm{el}}/\mu_0 J_0^2}$ |
| Turnover | $\tau_U$ | $L_0/U_0$ |
| Viscous diffusion | $\tau_\mu$ | $\rho_{\mathrm{el}} L_0^2/\mu$ |

where $\vec{F}_g$ and $\vec{F}_m$ are given by Eqs. (2) and (4), replacing the variables with their non-dimensional homologues. Characteristic times and non-dimensional numbers are shown in Tables 1 and 2. The Reynolds number computed from the fluid's viscosity would be of the order of $10^4$, but an estimation of the turbulent transport coefficient [2] implies that our corresponding Reynolds number is rather of the order of $10^2$. It can be regarded as a turbulent Reynolds number and thus roughly accounts for non-resolved turbulent scales.

### 2.6. Boundary conditions

Since the discontinuities in the transport coefficients of Eqs. (11) and (12) are assumed to be smooth (see Section 3), the boundary conditions at the interface need not be explicit. However, on the boundary $\partial\Omega$ of the simulation domain $\Omega$ corresponding to the inside of the cell, the following conditions hold.

*Velocity field.* Neglecting the inclined ledges, the frozen bath and the carbon walls roughness, we have no-slip, solid boundaries:

$$\vec{v}|_{\partial\Omega} = 0.$$

*Pressure.* Since the boundary conditions on $\vec{e}_n \cdot \vec{v}$ are imposed while solving for the viscous term (see Section 4.6), before performing projection (see Section 4.4), we want the pressure gradient to have no effect on the normal component of $\vec{v}$:

$$\vec{e}_n \cdot \vec{\nabla} p|_{\partial\Omega} = 0.$$

*Magnetic vector potential.* As stated previously, we assume the vertical walls to be insulating and the electrolysis current to be imposed at horizontal walls, so that the current disturbance cannot penetrate the boundaries:

$$\vec{e}_n \cdot \vec{j}|_{\partial\Omega} = 0 \Rightarrow \vec{e}_n \cdot (\vec{\nabla} \times \vec{b})|_{\partial\Omega} = 0. \tag{13}$$

Then, we consider the ferromagnetic shell enclosing the cell, assuming that the carbon wall between the liquid boundary and this shell is thin enough. The continuity of the tangential magnetic field approximates as $\vec{e}_n \times \vec{B}_{\text{shell}}/\mu_{\text{shell}} \simeq \vec{e}_n \times \vec{B}/\mu_0$ on $\partial\Omega$, where $\mu_0/\mu_{\text{shell}} \ll 1$, since the shell is ferromagnetic. Therefore, the tangential components of the magnetic field are limited in magnitude on the liquids side of the wall. While $\vec{B}_{\text{bg}}$ is the part of the external field not shielded by the shell, it is reasonable to assume that the tangential components of the disturbance $\vec{b}$ remain significantly weaker than those of $\vec{B}_{\text{bg}}$, and regarding Eq. (13), take a constant value on the boundary, hence we set:

$$\vec{e}_n \times \vec{b}|_{\partial\Omega} = 0 \Rightarrow (\vec{e}_n \cdot \vec{\nabla})(\vec{e}_n \cdot \vec{b})|_{\partial\Omega} = 0. \tag{14}$$

The second condition follows from $\vec{\nabla} \cdot \vec{b} = 0$.
Recalling that $\vec{\nabla} \cdot \vec{a} = 0$, we see that the conditions (14) can be satisfied by requiring

$$\vec{e}_n \cdot \vec{a}|_{\partial\Omega} = 0 \quad \text{and} \quad (\vec{e}_n \cdot \vec{\nabla})(\vec{e}_n \times \vec{a})|_{\partial\Omega} = 0. \tag{15}$$

*Electric potential.* Using a similar argument as for the pressure, we observe that the boundary conditions on $\vec{e}_n \cdot \vec{a}$ are imposed while solving for the diffusion term and we set:

$$\vec{e}_n \cdot \vec{\nabla} \varphi|_{\partial\Omega} = 0.$$

Table 2
Non-dimensional numbers

| Number | Symbol | Definition | Value |
|---|---|---|---|
| Interaction parameter | $N$ | $\tau_U^2/\tau_m^2$ | 1 |
| Froude | $Fr$ | $\tau_g/\tau_U$ | 0.11 |
| Magnetic Reynolds | Rm | $\tau_\eta/\tau_U$ | $9.1 \times 10^{-2}$ (aluminum)<br>$9.1 \times 10^{-6}$ (bath) |
| Reynolds | $Re$ | $\tau_\mu/\tau_U$ | 500 |

## 3. Level set method

In order to track the interface between the two liquids and to account for their different transport coefficients, we advect a function $\phi$ whose zero-level implicitly defines the location of the interface:

$$\frac{\partial \phi}{\partial t} = -\vec{\nabla} \cdot (\vec{v}\phi), \tag{16}$$

thus passively propagating the zero-level along the flow. This is known as a level set method [22].

As shown in Fig. 3, the level set function $\phi$ must be positive in one fluid and negative in the other, so that any fluid-dependent physical property, such as the mass density $\rho$, can be obtained at some given point $P$ in the following manner:

$$\rho(P) = H_\epsilon(\phi(P))\rho_{\text{al}} + [1 - H_\epsilon(\phi(P))]\rho_{\text{el}},$$

where $\rho_{\text{al}}$ and $\rho_{\text{el}}$ are the mass densities of aluminum and electrolytic bath, respectively. $H_\epsilon(\phi)$ is a smooth approximate to Heaviside's step function $H_0(\phi)$, and it is defined as [23]:

$$H_\epsilon(\phi) = \begin{cases} 1 & \text{if } \phi > \epsilon, \\ 0 & \text{if } \phi < -\epsilon, \\ \frac{1}{2}\left[1 + \frac{\phi}{\epsilon} + \frac{1}{\pi}\sin\left(\frac{\pi\phi}{\epsilon}\right)\right] & \text{otherwise,} \end{cases} \tag{17}$$

where the parameter $\epsilon$ stands as an effective interface width, as shown in Fig. 4. Here, we take this width to be proportional to the vertical grid step ($\Delta z$), since the interface is mainly horizontal. We observed, on an empirical basis, that a value of $\epsilon = 1.5\Delta z$ keeps the scheme stable, given the magnitude of the discontinuities.

In order for the interface width $\epsilon$ from Eq. (17) to make sense, $H_\epsilon(\phi)$ must run exactly from value 0, at distance $\epsilon$ from the interface on one side, to value 1, at the same distance on the other side. That is, $\phi$ must run from $-\epsilon$ to $\epsilon$ on the same range, i.e. $\phi$ has to be a signed distance function. This means that, in addition to being positive on one side of the interface and negative on the other, it must satisfy

$$\|\vec{\nabla}\phi\| = 1. \tag{18}$$

This can be achieved thanks to a *redistancing* algorithm [23], which resets any level set function $\phi$ as a signed distance function, with the side effect of improving numerical mass conservation by eliminating steep gradients of $\phi$ near the interface. Thus, after each time integration step of Eq. (16), the level set function is reset to a signed distance function. First, $\phi_0$ is set to the value of $\phi$ before redistancing and then the following equation is solved:

$$\frac{\partial \phi}{\partial \tau} = \mathscr{L}(\phi_0, \phi), \tag{19}$$

where $\tau$ is some artificial time and

$$\mathscr{L}(\phi_0, \phi) \equiv (1 - \|\vec{\nabla}\phi\|)\text{sign}_\epsilon(\phi_0). \tag{20}$$

Eq. (19) reaches its steady-state when Eq. (18) is satisfied. The sign function, whose purpose is to preserve the sign of $\phi_0$ without changing its zero-level, is defined as

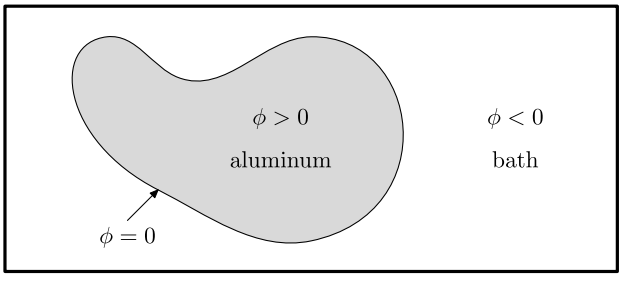


Fig. 3. Level set method.

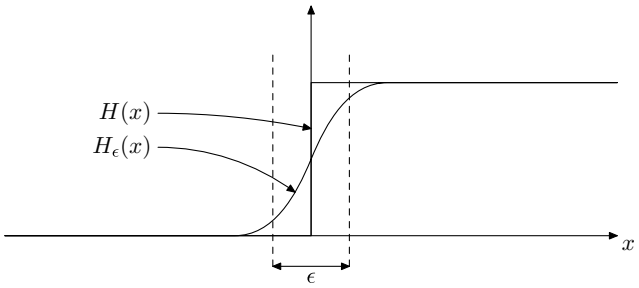


Fig. 4. Smooth Heaviside function.

$$\mathrm{sign}_\epsilon(x) = 2H_\epsilon(x) - 1.$$

The gradient operator in Eq. (20) is discretized using a first-order[1] upwind scheme [24]:

$$\frac{\partial\phi}{\partial x_j} \simeq \begin{cases} D_j^+\phi & \text{if } \mathrm{sign}_\epsilon(\phi_0)D_j^+\phi < 0 \quad \text{and} \quad \mathrm{sign}_\epsilon(\phi_0)(D_j^+ + D_j^-)\phi < 0, \\ D_j^-\phi & \text{if } \mathrm{sign}_\epsilon(\phi_0)D_j^-\phi > 0 \quad \text{and} \quad \mathrm{sign}_\epsilon(\phi_0)(D_j^+ + D_j^-)\phi > 0, \\ 0 & \text{if } \mathrm{sign}_\epsilon(\phi_0)D_j^+\phi > 0 \quad \text{and} \quad \mathrm{sign}_\epsilon(\phi_0)D_j^-\phi < 0, \end{cases}$$

where $D_j^+$ and $D_j^-$ are the standard forward and backward first-order finite differences along axis $x_j$. The use of such a scheme is necessary to preserve the interface's position as well as to reach the steady-state of Eq. (19). It has been proved [25] that $\phi$ can be correctly redistanced within a radius $\alpha\Delta x$ when Eq. (19) is integrated over a time $\Delta\tau = \alpha\Delta x$. It further has been shown that $\Delta\tau$ is a valid time step for integration. Thus, a few iterations are enough to make $\phi$ a signed distance function in the neighborhood of the interface, which is indeed the only domain where Eq. (18) has to be verified. In fact, there is a volume conservation problem inherent to this redistancing technique [25]. For each control volume $\mathscr{V}$, a corrective term must be appended to Eq. (19):

$$\frac{\partial\phi}{\partial\tau} = \mathscr{L}(\phi_0, \phi) + \lambda f(\phi),$$

where $\lambda$ and $f(\phi)$ depend on $\mathscr{V}$ and have to be defined such that the following constraint be satisfied:

$$\frac{\partial}{\partial\tau}\int_{\mathscr{V}} H_\epsilon(\phi)\,\mathrm{d}V = 0,$$

i.e. the volume (of aluminum) enclosed by the interface has to be conserved within the control volume $\mathscr{V}$. Differentiating the above equation results in:

$$\int_{\mathscr{V}} H'_\epsilon(\phi)\frac{\partial\phi}{\partial\tau}\mathrm{d}V = \int_{\mathscr{V}} H'_\epsilon(\phi)[L(\phi_0, \phi) + \lambda f(\phi)]\mathrm{d}V = 0.$$

Thus, an expression for $\lambda$ can be obtained:

$$\lambda = \frac{-\int_{\mathscr{V}} H'_\epsilon(\phi_0)L(\phi_0, \phi)\,\mathrm{d}V}{\int_{\mathscr{V}} H'_\epsilon(\phi_0)f(\phi)\,\mathrm{d}V}. \tag{21}$$

Then, choosing

$$f(\phi) \equiv H'_\epsilon(\phi)\|\phi\|$$

allows the correction to be made only at the interface and thus preserves Eq. (18) elsewhere: the derivative $H'_\epsilon$ of the smooth Heaviside's function $H_\epsilon$ is in fact a smooth approximate of Dirac's distribution $\delta$. So, $f(\phi)$ and thus the correction to Eq. (19) are null everywhere but at the interface. Finally, Eq. (21) becomes:

[1] Other spatial derivatives in our scheme are discretized at second-order. The purpose of the redistancing process is just to keep the slope of $\phi$ of order unity; it involves no physical process.

$$\lambda = \frac{-\int_{\mathscr{V}} H'_\epsilon(\phi_0) L(\phi_0, \phi)\,\mathrm{d}V}{\int_{\mathscr{V}} [H'_\epsilon(\phi_0)]^2 \|\vec{\nabla}\phi_0\|\mathrm{d}V}.$$

This summarizes the approach proposed by Sussman and Fatemi [25]. For the integrals in the last equation, we use the same discretization as when dealing with averages (see Section 4.3), but without normalizing by the volume.

## 4. Discretization

### 4.1. Staggered grids

The fields $\vec{v}$, $\vec{a}$, $p$, $\varphi$and $\phi$ are defined at discrete locations on a fixed regular mesh, whose control volume of size $\Delta x \times \Delta y \times \Delta z$ is illustrated in Fig. 5. The velocity and magnetic vector potential fields components are staggered on the faces of this control volume, while all other quantities are defined in the center. This allows for an exact projection (see Section 4.4).

### 4.2. Finite volumes

The momentum conservation Eq. (1) is written in conservative form:

$$\frac{\partial \rho \vec{v}}{\partial t} = Q - \vec{\nabla} \cdot \vec{J},$$

where $Q$ is a source (sink) term and $\vec{J}$ is the momentum flux density. Integrating over a control volume $\mathscr{V}$ bounded by the closed surface $\partial\mathscr{V}$ and normalizing by its volume $V = \Delta x \Delta y \Delta z$ yields:

$$\frac{\mathrm{d}\overline{\rho\vec{v}}}{\mathrm{d}t} = \overline{Q} - \frac{1}{V}\oint_{\partial\mathscr{V}} \vec{J} \cdot \mathrm{d}\vec{a}, \tag{22}$$

where the upper bar $\bar{\cdot}$ denotes the average.

Since the control volume is rectangular, the surface integral in Eq. (22) reduces to a sum of the face-averaged components of $\vec{J}$ (see Fig. 6):

$$\frac{1}{V}\oint_{\partial\mathscr{V}} \vec{J} \cdot \mathrm{d}\vec{a} = \sum_{k=1}^{3} \frac{\overline{J_k^+} - \overline{J_k^-}}{\Delta x_k}.$$

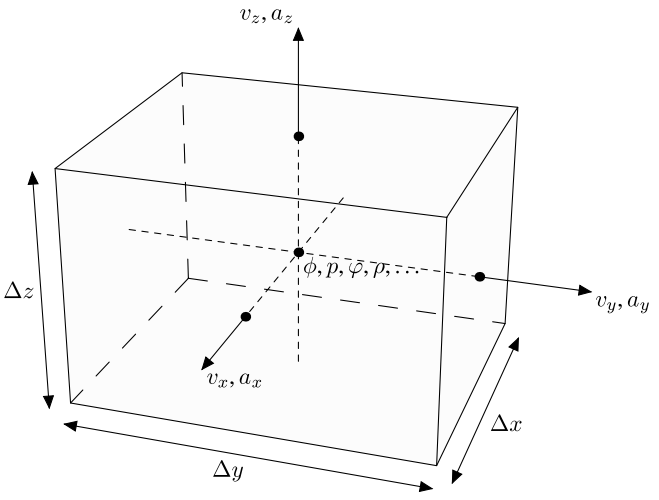


Fig. 5. Control volume.

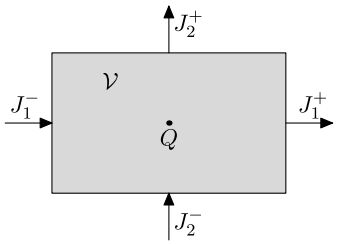


Fig. 6. Finite-volume method (2D cut).

### 4.3. Averaging and reconstruction

After time integration of Eq. (22), one has to recover the point values of $\rho\vec{v}$ from $\overline{\rho\vec{v}}$. This leads to a reconstruction process. We define the (independent) averaging operators $\mathscr{A}_1$, $\mathscr{A}_2$ and $\mathscr{A}_3$ along each axis inside the control volume $\mathscr{V}$, such that

$$\overline{\rho\vec{v}} = \mathscr{A}_1\mathscr{A}_2\mathscr{A}_3\rho\vec{v} \tag{23}$$

and, e.g.

$$\overline{J_1^+} = \mathscr{A}_2\mathscr{A}_3 J_1^+. \tag{24}$$

Next, we define the corresponding inverse operators $\mathscr{R}_1 = \mathscr{A}_1^{-1}$, $\mathscr{R}_2 = \mathscr{A}_2^{-1}$ and $\mathscr{R}_3 = \mathscr{A}_3^{-1}$ for reconstruction of point values. Now, substituting Eqs. (23) and (24) in Eq. (22), then applying 3D reconstruction $\mathscr{R}_1\mathscr{R}_2\mathscr{R}_3$ results in the following average-free equation:

$$\frac{\partial\rho\vec{v}}{\partial t} = Q - \sum_{k=1}^{3}\frac{\mathscr{R}_k(J_k^+ - J_k^-)}{\Delta x_k}.$$

This method avoids some unwanted numerical diffusion from the usual averaging–reconstruction cycle. Reconstruction is achieved using 3-point stencils derived from Taylor expansions of the averages around the reconstructed point.

### 4.4. Projection

To enforce the $\vec{\nabla}\cdot\vec{v} = 0$ and $\vec{\nabla}\cdot\vec{a} = 0$ conditions, we solve for $p$ and $\varphi$ by Hodge–Helmholtz decomposition, using a projection method with staggered grids. See [26] for a complete description of the method used and [27] for the treatment of stencils with variable density.

### 4.5. Time integration

Time integration is achieved using a fully explicit second-order Adams–Bashforth (AB2) scheme for most terms of Eqs. (11) and (12): $f^{n+1} = f^n + \Delta t(3f_t^n - f_t^{n-1})/2$, where $f^n$ denotes the value of the discrete field $f$ at the $n$th time step, and $f_t$, the time derivative of $f$. The first time step is achieved with a forward Euler scheme. The AB2 scheme is known to be stable and weakly dispersive [28]. It is thus well suitable for simulating a wave-generating system such as the aluminum reduction cell with interfacial waves. There are, however, two exceptions to the use of AB2. First, for the viscous term, a second-order semi-implicit Crank–Nicolson (CN) scheme is used: $f^{n+1} = f^n + \Delta t(f_t^n + f_t^{n+1})/2$. Second, since the coefficient of the magnetic diffusion term takes a very large value inside the electrolytic bath, it makes no sense to advance it with an explicit scheme, hence the unconditionally stable first-order backward Euler (BE) scheme has been chosen: $f^{n+1} = f^n + \Delta t f_t^{n+1}$.

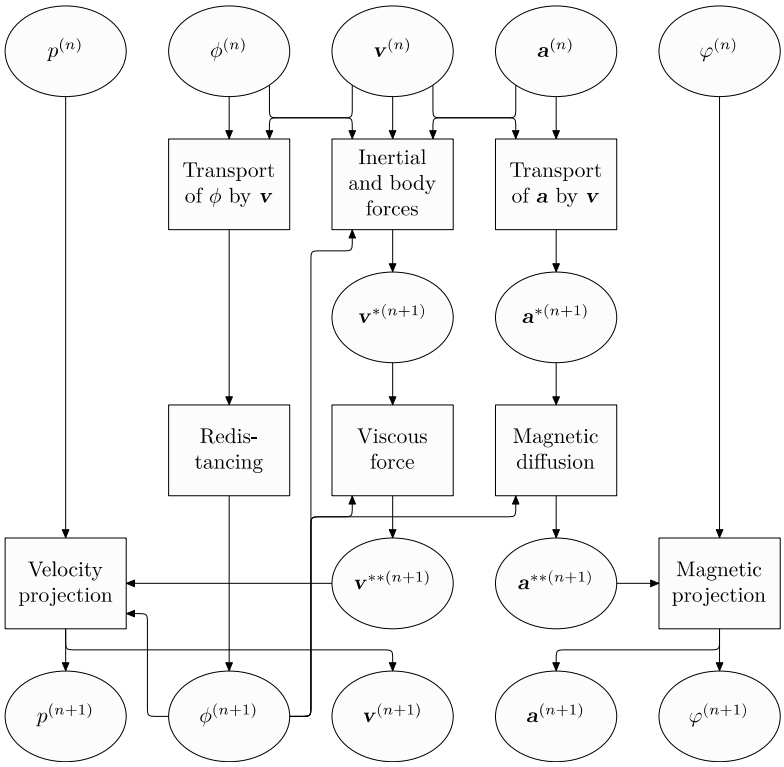


Fig. 7. Algorithm dependencies.

### 4.6. Overall algorithm

The dependencies are illustrated in Fig. 7. The method can be summarized as follows:

(1) Transport of the level set function $\phi$.
(2) Redistancing of $\phi$ about the interface.
(3) Partial transport of the momentum density $\rho\vec{v}$.
(4) Implicit viscous term solver (GMRES).
(5) Projection of $\vec{v}$ into the space of solenoidal fields (GMRES).
(6) Partial transport of $\vec{a}$ (GMRES).
(7) Implicit resolution of the magnetic diffusion term (GMRES).
(8) Projection of $\vec{a}$ into the space of solenoidal fields (GMRES).

We use the PETSc library's [29] implementation of the generalized minimal residual (GMRES) iterative solver, preconditioned with a symmetric successive over relaxation (SSOR) factorization.

## 5. Tests and results

This section discusses some results computed using the numerical method describe above. In the first two tests, magnetic effects are turned off in order to investigate the hydrodynamic (HD) reliability of the code only. The last two tests concern MHD aspects.

### 5.1. Test 1: Single-fluid hydrodynamics. Homogeneous turbulence

In this test, we simulate a forced turbulent single-fluid but incompressible viscous flow inside a cubic box of size $L_0$, at different resolutions $n \equiv n_x = n_y = n_z$, ranging from 30 to 160 grid points along each direction. The

numerical Reynolds number (as defined in Eq. (11) and Table 2), is $Re = 500$. Spectral forcing of random orientation is applied to the largest scales, with an energy injection rate kept constant regardless of the resolution. The following analysis displays the properties of the flow averaged over 25 mean turnover times. Average kinetic energy spectra (Fig. 8) show that numerically underresolved flows accumulate energy that can not be dissipated. However, the dissipation tails of the spectra do not change anymore for resolutions larger than 100, as the smallest scales become better resolved. Depending on the resolution, the turbulent Reynolds number takes different average values (Fig. 9), decreasing from $Re_t \approx 200$ and stabilizing around $Re_t \approx 110$ for the highest resolutions. This is in agreement with the spectra shown in Fig. 8. The turbulent Reynolds number is computed as $Re_t = u_0 l_0/v$, in terms of the rms velocity $u_0$ and the integral scale

$$l_0 = 2\pi \frac{\int e_k/k \, \mathrm{d}k}{\int e_k \, \mathrm{d}k},$$

where $e_k$ is the spectral energy density at wavelength $k$. The slight increase of $l_0$ (Fig. 9) is expected for higher resolutions because the numerical grid viscosity is weaker [30] but it does not change much for $n$ above 120 and this is also the case for the energy transfer rate $\epsilon = u_0^3/l_0$ (Fig. 9). The convergence of the physical properties of the flow for high $n$ reveals that, despite a small residual amount of energy accumulating in the tail of each spectrum, there are enough grid points to account for all relevant scales. Simulating the whole dissipative range [31] is not an easy task and it may not be always necessary [32].

### 5.2. Test 2: Two-fluid hydrodynamics. Pure gravity modes

We now simulate a two-fluid flow but we still do not consider the magnetic effects. The dispersion relation derived by Sneyd [5] for shallow layers (long waves) reduces, in this case, to the following interfacial gravity wave dispersion relation:

$$\omega = -\mathrm{i}\frac{\gamma}{2} \pm \sqrt{\frac{\Delta\rho g k}{\rho_{\mathrm{al}} \coth kH_{\mathrm{al}} + \rho_{\mathrm{el}} \coth kH_{\mathrm{el}}} - \frac{\gamma^2}{4}},$$

where $\gamma$ is a damping factor depending on linear friction terms in both layers, while $H_{\mathrm{al}}$ and $H_{\mathrm{el}}$ refer to the respective equilibrium depths of aluminum and bath.

In our three-dimensional case, there is no linear friction but rather viscous effects and no-slip boundary conditions. To keep things simple for purposes of numerical testing, we set the physical viscosity to a value low enough so that we can assume $\gamma = 0$ in the above dispersion relation. At initial time in an 8:1-aspect ratio cell, the velocity field is null and the interface is given the sinusoidal shape of a single mode. Then we compute the wave frequencies based on the period of the first oscillation, for two different resolutions: $n_x = 60$, $n_z = 40$, and $n_x = 80$, $n_z = 80$. This is shown in Fig. 10. The relative error for both resolutions remains below 3% for all

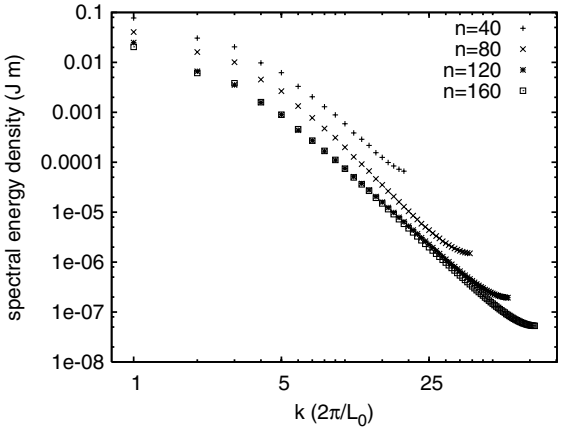


Fig. 8. Test 1: Hydrodynamic single-fluid turbulence. Kinetic energy spectrum versus the normalized wavenumber, in logarithmic scale, for different numbers $n \equiv n_x = n_y = n_z$ of grid points along each axis.

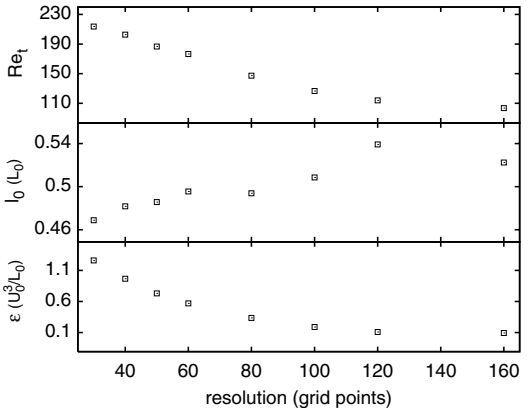


Fig. 9. Test 1: Hydrodynamic single-fluid turbulence. (From top to bottom) Turbulent Reynolds number $Re_t$, integral scale $l_0$ in units of $L_0$, and kinetic energy transfer rate $\epsilon$ in units of $U_0^3/L_0$.

wavenumbers up to $k = 8\pi/L_x$. Wavenumbers greater than $8\pi/L_x$ are less relevant in the context of long waves theory, because in such cases, nonlinear effects arise.

### 5.3. Test 3: Single-fluid MHD. Diffusion along the magnetic field

In this test, we consider the turbulent flow of a single fluid subject to a strong vertical uniform external magnetic field. Theory [33] predicts that in such a situation, momentum is expected to diffuse along the magnetic field lines, so that the vortices elongate and the flow becomes anisotropic. The horizontal layers near the top and bottom walls become strongly correlated within a characteristic time $\tau_{2D} = \rho L_z^2/\sigma B_{bg}^2 L_x^2$. With our scaling and definitions from Table 1, this is equivalent to $\tau_{2D} = (\tau_m^2/\tau_\eta)(L_z/L_x)^2/\beta = \tau_m/\beta \mathrm{Rm}$, where $\beta$ is the dimensionless magnitude of the background magnetic field, in units as chosen in Section 2.5.

We performed simulations of a large scale decaying random turbulent flow in a cubic box of size $L_0$ with a background uniform vertical magnetic field given by

$$\vec{B}_{bg} = \beta\mu_0 J_0 L_0 \vec{e}_z. \tag{25}$$

The purpose is to compare the horizontal and vertical correlation lengths which we define, respectively, as

$$l_h = 2\pi \frac{\int e_{\vec{k}}/\sqrt{k_x^2 + k_y^2}\, d^3\vec{k}}{\int e_{\vec{k}}\, d^3\vec{k}} \quad \text{and} \quad l_z = 2\pi \frac{\int e_{\vec{k}}/k_z\, d^3\vec{k}}{\int e_{\vec{k}}\, d^3\vec{k}}.$$

Simulations were carried out for three different magnitudes of the background magnetic field $B_{bg} = \beta\mu_0 J_0 L_0$. The behavior of the ratio $l_h/l_z$ versus the normalized time $t/\tau_{2D}$, plotted in Fig. 11, is in agreement with theory [33]: after time $\tau_{2D}$, the vortices are spread vertically and $l_h/l_z$ reaches a steady-state, corresponding to an

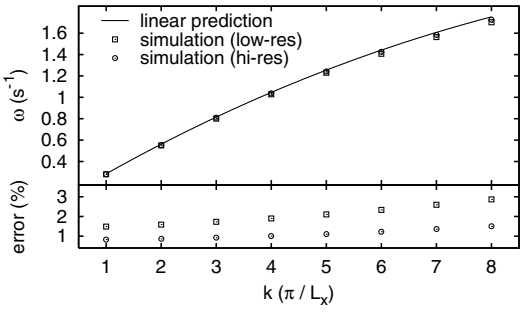


Fig. 10. Test 2: Pure gravity modes. Dispersion relation as predicted by linear theory (solid line) and as computed for an 8:1 aspect ratio with two different resolutions ($n_x = 60$, $n_z = 40$ (□)) and ($n_x = 80$, $n_z = 80$ (○)) is shown at top. Relative error between computed and predicted values is shown at bottom.

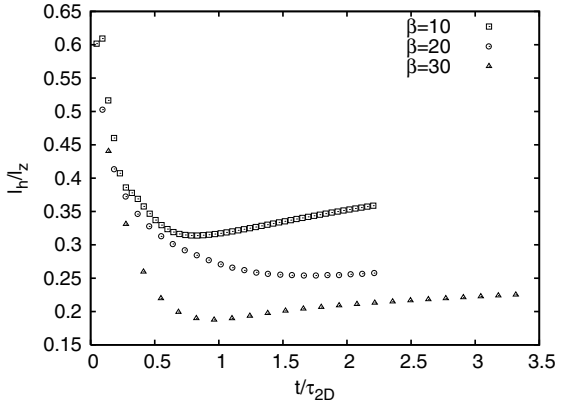


Fig. 11. Test 3: Single-fluid MHD. This plot shows the evolution of the momentum anisotropy versus time under a given external magnetic field. The ratio of the horizontal scale $l_h$ to the vertical scale $l_z$ is plotted against the normalized time $t/\tau_{2D}$ for three different magnitudes of the background vertical magnetic field. Around $t = \tau_{2D}$, the anisotropy reaches a nearly steady-state as predicted by theory [33].

equilibrium between the diffusion of momentum along the magnetic field lines and the restoration of isotropy by nonlinear inertial effects.

### 5.4. Test 4: Two-fluid MHD. Metal pad roll

The fourth test regards MHD interfacial gravity waves at low magnetic Reynolds number. This simultaneously accounts for all of the previous features. Observations [34] suggest that a uniform vertical background field has important effects on the flow stability [6,7,9]. Therefore, as in Gerbeau et al. [13], we consider such a background magnetic field given by Eq. (25). In this context, the dimensionless parameter $\beta$ is a measure of the relative intensity of the background field in terms of that induced by the imposed current $\vec{J}_0$. We have further considered an equal depth of aluminum and bath. In order to be able to compute the flow, we had to reduce the electrical conductivity jump by taking $\mathrm{Rm}_{\mathrm{el}} = 10^{-3}$ in the electrolytic bath. We believe that this approximation has no important physical drawback, since the $\mathrm{Rm}_{\mathrm{el}} \ll \mathrm{Rm}_{\mathrm{al}} < 1$ property is preserved. Following Sneyd and Wang [8], the vertical displacement of the interface $\zeta(x, y)$ is expanded into a cosine series:

$$\zeta(x,y) = \sum_{m,n} a_{mn}(t) \cos\frac{m\pi x}{L_x} \cos\frac{n\pi y}{L_y}.$$

We now focus on the results from our simulations in a square cell of aspect ratio 3:3:1. At time $t = 0$, all velocity components are set to zero. A perturbation $\zeta(x, y)$ of the interface is set to $a_{10} = -0.025L_0$, i.e. the first $x$-mode is perturbed by a factor of 2.5%. All other coefficients $a_{mn}$ are set to zero. As expected, the amplitude of the first $y$-mode, which is the most strongly coupled mode to $a_{10}$, grows during the first oscillations. Later, when the flow has reached a steady-state, $a_{10}$ and $a_{01}$ dominate, while all other coefficients have remained two orders of magnitude below. Coefficients $a_{10}$ and $a_{01}$ are plotted in Fig. 12, for two different magnitudes of $B_{\mathrm{bg}}$. The roll being a rotating wave, the trajectory through phase space becomes perfectly round after a dozen of oscillations in the stable case, i.e. $a_{10}$ and $a_{01}$ are of same amplitude but the two phases are shifted by $\pi/2$, the modes being in resonance together. Our results are qualitatively the same as in Gerbeau et al. [13] in that the roll appears, is stable for weak vertical magnetic field, and unstable for a strong one. However, in their study, some parameters were slightly different than ours, with corresponding non-dimensional numbers $Re = 1000$, $Fr = 1.2$, $\mathrm{Rm}_{\mathrm{al}} = 1$ and $\mathrm{Rm}_{\mathrm{el}} = 10^{-4}$. It is to be noted that even though our method does not allow for the $10^4$ conductivity ratio as opposed to the ALE approach [13], we still achieve a high precision tracking of the interface.

In another simulation, we used a rectangular cell of aspect ratio 12:4:1, a background magnetic field of $B_{\mathrm{bg}} = 3.27$ mT, and initial conditions $a_{30} = -0.025L_0$, all other cosine coefficients $a_{mn}$ being null. The dominant modes $a_{30}$ and $a_{01}$ are plotted in Fig. 13. As opposed to the square cell, there are also other modes, weaker though non-negligible, namely $a_{21}$ and $a_{51}$ followed by $a_{41}$. For this simulation, with a resolution of $n_x \times n_y \times n_z = 120 \times 40 \times 20 = 96{,}000$ grid points, the integration of one turnover time $\tau_U = \tau_{\mathrm{m}}$, as defined in

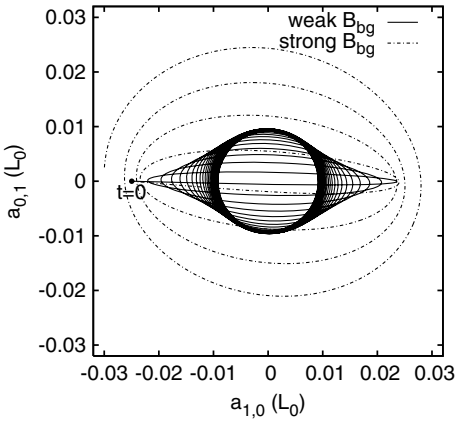


Fig. 12. Test 4: Two-fluid MHD flow: metal pad roll instability. Evolution in time of the first $a_{0,1}$ and $a_{1,0}$ modes of the interface vertical displacement, in units of $L_0$, during the metal pad roll in an aspect ratio 3:3:1 cell. The rotating wave is stable for a weak background field ($\beta = 0.3$, total integration time of 4 min 28 s) and unstable for a stronger ($\beta = 1.0$, integration time of 36 s).

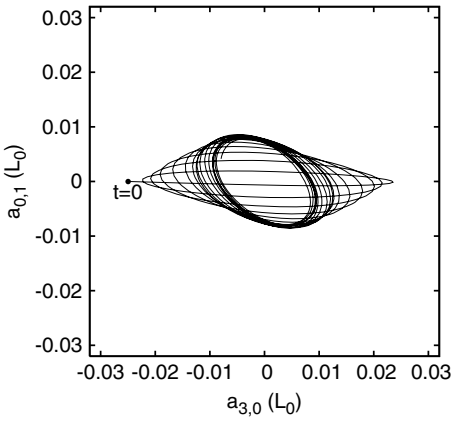


Fig. 13. Test 4: Metal pad roll. Evolution in time of the dominant modes $a_{0,1}$ and $a_{3,0}$ of the interface vertical displacement, in units of $L_0$, during the metal pad roll in a cell of aspect ratio 12:4:1. The total integration time is 3 min 17 s.

Table 1, takes 2 h in CPU time on a small AMD Athlon XP 1700+ machine, the biggest part of the time being spent in the GMRES solver. Since the PETSc library is MPI-ready, our code could be readily parallelized.

## 6. Conclusion

We have combined a three-dimensional finite-volume method with a level set technique to simulate the MHD instabilities in aluminum reduction cells. In our model, the magnetic and current fields are both split into a constant part and a flow-dependent disturbance. Keeping $\vec{\nabla} \cdot \vec{b} = 0$ is achieved by writing the equations and making the computations in terms of the magnetic vector potential $\vec{a}$ instead of the magnetic field itself. The gauge condition $\vec{\nabla} \cdot \vec{a} = 0$ is enforced by using the same exact projection scheme on $\vec{a}$ as on $\vec{v}$, both fields being defined on staggered grids.

The code has been subject to four series of tests: (1) HD turbulence and (2) HD interfacial gravity waves; then (3) MHD growth of anisotropy in a single fluid, and finally (4) the metal pad roll. The purpose of this fourfold testing was to verify that the code behaves correctly in single-fluid HD and MHD regime, as well as in two-fluid HD conditions, before considering two-fluid MHD. It is found in test 1 that the kinetic energy spectra, the turbulent Reynolds number and the integral scale of turbulence converge at sufficiently high

resolution. In test 2, the computed gravitational wave frequencies are in very good agreement with the ones predicted by the linear shallow-layers theory. Test 3 showed that momentum diffuses along the magnetic field lines during the time scale estimated from low-Rm theory. With the last test (4), the code has proven to be able to successfully reproduce a well-known regime of flow in aluminum reduction cells, namely the metal pad roll. We believe that our method can be used with a good level of confidence to investigate MHD instabilities in two-fluid flows.

## Acknowledgments

This research has been supported by *Alcan International Ltd.* and the *Natural Sciences and Engineering Research Council of Canada*, from which the first author has been granted a scholarship. Most of the computations were performed on computers of the *Réseau Québécois de Calcul Haute Performance*. The authors are grateful to Thierry Tomasino from *Alcan CRV* and to Tony Lelièvre from the *Centre d'Enseignement et de Recherche en Mathématiques, Informatique et Calcul Scientifique*, at *École nationale des ponts et chaussées* for enlightening discussions about their numerical methods. The authors also wish to thank both referees for their interesting remarks and conscientious review.

## References

[1] K. Grjotheim, C. Krohn, M. Malinovsky, K. Matiasovsky, J. Thonstad, Aluminum Electrolysis, second ed., Aluminium-Verlag, Dusseldorf, 1982.
[2] N. Urata, K. Mori, H. Ikeuchi, Behavior of bath and molten metal in aluminum electrolytic cell, J. Jpn. Institut. Light Metals 26 (11) (1976) 573–583.
[3] R. Moreau, J.W. Evans, An analysis of the hydrodynamics of aluminum reduction cells, J. Electrochem. Soc. 131 (10) (1984) 2251–2259.
[4] A.D. Sneyd, Stability of fluid layers carrying a normal electric current, J. Fluid Mech. 156 (1985) 223–236.
[5] A.D. Sneyd, Interfacial instabilities in aluminium reduction cells, J. Fluid Mech. 236 (1992) 111–126.
[6] T. Sele, Instabilities of the metal surface in electrolytic alumina reduction cells, Metall. Trans. B 8B (1977) 613–618.
[7] V. Bojarevičs, M. Romerio, Long wave instability of liquid metal–electrolyte interface in aluminium electrolysis cells: a generalization of Sele's criterion, Eur. J. Mech. B 13 (1) (1994) 33–56.
[8] A.D. Sneyd, A. Wang, Interfacial instability due to MHD mode coupling in aluminium reduction cells, J. Fluid Mech. 263 (1994) 343–359.
[9] P.A. Davidson, R.I. Lindsay, Stability of interfacial waves in aluminium reduction cells, J. Fluid Mech. 362 (1998) 273–295.
[10] K. Mori, K. Shiota, N. Urata, H. Ikeuchi, The surface oscillation of liquid metal, Light Metals 11 (1976) 77–95.
[11] L. Leboucher, K. Pericleous, I. Panaitescu, M. Repetto, A finite-volume shallow layer method, for the MHD instabilities in an aluminium production cell, in: Proceedings of the Second International Conference on CFD in the Minerals and Process Industries, Melbourne, Australia, 1999, pp. 335–338.
[12] V. Potočnik, Modelling of metal–bath interface waves in Hall–Heroult cells using ESTER/PHOENICS, Light Metals (1989) 227–235.
[13] J.-F. Gerbeau, C. Le Bris, T. Lelievre, Simulations of MHD flows with moving interfaces, Tech. rep., INRIA, 2001.
[14] R.J. Moreau, D. Ziegler, The Moreau–Evans hydrodynamic model applied to actual Hall–Héroult cells, Metall. Trans. B 19B (1988) 737–744.
[15] P. Kundu, Fluid Mechanics, second ed., Academic Press, New York, 2002.
[16] P.A. Davidson, An Introduction to Magnetohydrodynamics, Cambridge University Press, Cambridge, 2001.
[17] R.J. LeVeque, D. Mihalas, E. Dorfi, E. Mueller, Nonlinear conservation laws and finite volume methods for astrophysical fluid flow, lecture notes, O. Steiner, A. Gautschy, 27th Saas-Fee Advanced Course Lecture Notes, Springer, Berlin, 1998.
[18] D. Munger, A. Vincent, Numerical simulation of the magnetohydrodynamic instabilities in aluminium reduction cells, in: Proceedings of the 12th Annual Conference of the CFD Society of Canada, Ottawa, Canada, 2004, pp. 571–578.
[19] A. Dedner, F. Kemm, D. Kröner, C.-D. Munz, T. Schnitzer, M. Wesenberg, Hyperbolic divergence cleaning for the MHD equations, J. Comput. Phys. 175 (2002) 645–673.
[20] A. Dedner, D. Kröner, C. Rohde, M. Wesenberg, Efficient divergence cleaning in three-dimensional MHD simulations. in: E. Krause, W. Jäger (Eds.), High Performance Computing in Science and Engineering '02, 2003, pp. 323–334.
[21] R.K. Wangsness, Electromagnetic Fields, second ed., Wiley, New York, 1986.
[22] S. Osher, J.A. Sethian, Fronts propagating with curvature-dependent speed: algorithms based on Hamilton–Jacobi formulations, J. Comput. Phys. 79 (1988) 12–49.
[23] M. Sussman, P. Smereka, S. Osher, A levelset approach for computing solutions to incompressible two-phase flow, J. Comput. Phys. 114 (1994) 146–159.
[24] C.W. Shu, S. Osher, Efficient implementation of essentially non-oscillatory shock-capturing schemes, II, J. Comput. Phys. 83 (1989) 32–78.

[25] M. Sussman, E. Fatemi, An efficient, interface preserving level set re-distancing algorithm and its application to interfacial incompressible fluid flow, SIAM J. Sci. Comput. 20 (4) (1999) 1165–1191.
[26] J.H. Ferziger, M. Perić, Computational Methods for Fluid Dynamics, third ed., Springer, Berlin, 2002.
[27] W.J. Rider, Approximate projection methods for incompressible flows: implementation, variants and robustness, Tech. rep., Los Alamos National Laboratory, 1995.
[28] C. Canuto, M.Y. Hussaini, A. Quarteroni, T.A. Zang, Spectral Methods in Fluid Dynamics, Springer, Berlin, 1987.
[29] S. Balay, W.D. Gropp, L.C. McInnes, B.F. Smith, Petsc home page. Available from: <http://www.mcs.anl.gov/petsc>, 2001.
[30] P. Roache, Computational Fluid Dynamics, Hermosa, Albuquerque, NM, 1976.
[31] S. Chen, G. Doolen, J.R. Herring, R.H. Kraichnan, S.A. Orszag, Z.S. She, Far-dissipation range of turbulence, Phys. Rev. Lett. 70 (20) (1993) 3051–3054.
[32] M. Meneguzzi, H. Politano, A. Pouquet, M. Zolver, A sparse-mode spectral method for the simulation of turbulent flows, J. Comput. Phys. 123 (1) (1996) 32–44, URL: http://dx.doi.org/10.1006/jcph.1996.0003.
[33] J. Sommeria, R. Moreau, Why, how, and when, MHD turbulence becomes two-dimensional, J. Fluid Mech. 118 (1982) 507–518.
[34] A.F. LaCamera, D.P. Ziegler, R.L. Kozarek, Magnetohydrodynamics in the Hall–Heroult process, an overview, Magnetohydrodyn. Process Metall. (1991) 91–98.